177ème Session du comité scientifique et technique de la Société Hydrotechnique de France Paper number: 04
Progrès récents des méthodologies de modélisation des écoulements diphasiques, Lyon, France, 24-26 novembre 2004.
Advances in the modelling methodologies of two-phase flows, Lyons, France, November 24-26, 2004.

VOLUME-OF-FLUID METHOD BASED NUMERICAL SIMULATIONS OF GAS-LIQUID TWO-PHASE FLOW IN CONFINED GEOMETRIES

Martin Wörner[1], Bradut E. Ghidersa, Milica Ilić, Dan G. Cacuci
Forschungszentrum Karlsruhe, Institut für Reaktorsicherheit, Postfach 3640, 76021 Karlsruhe, Germany, E-Mail: woerner@irs.fzk.de

KEY WORDS

Bubble train flow, square mini-channel, bubble induced turbulence, turbulence kinetic energy equation

ABSTRACT

In this paper we present results of volume-of-fluid method based direct numerical simulations of two types of gas-liquid flow in confined geometries. The first flow under consideration is the co-current upward flow of a regular train of gas bubbles within silicon oil in a square vertical mini-channel. Particular attention is given to the influence of the length of the flow unit cell and on the relation between bubble diameter and capillary number. The second type of flow under investigation is that of a swarm of eight bubbles within a narrow plane vertical channel. The numerical data are used to evaluate the budget of the turbulence kinetic energy equation for the liquid phase and to test common closure assumptions for the interfacial term appearing in this equation.

1. INTRODUCTION

Within the last decade great progress has been made in the development of advanced numerical methods for computation of gas-liquid flows with deformable interfaces. Among these methods for "direct numerical simulation" (DNS) of two-phase flow, the volume-of-fluid (VOF) method originally introduced by Hirt & Nichols (1981) has been significantly improved while the level-set method (Sussman *et al.*, 1994) and front-tracking method (Univerdi & Tryggvason, 1992) have newly emerged. Today's computer power is, however, far from what is needed to apply these methods for technical two-phase flow problems. Nevertheless, these methods have two main merits. First they allow to get a deeper insight into the underlying mechanisms of gas-liquid flows and thus foster their physical understanding. Second, they can provide a unique database of the three-dimensional velocity and pressure field and the phase distribution with high spatial and temporal resolution. Such a database can be used to develop and improve physical models for computational fluid dynamics (CFD) codes and engineering flow computations.

In this paper we exemplify both merits of two-phase DNS by considering two types of gas-liquid flows in confined geometry. In section 2 we first present the governing equations and give some details of the VOF method used to perform the numerical simulations. With respect to the first merit, i.e. the enhancement of the basic understanding of two-phase flows, simulations of the bubble train flow in a square vertical mini-channel are presented in section 3. With respect to the second merit, i.e. supporting the development of models for engineering computations, in section 4 DNS data of the rise of a bubble swarm within a narrow plane vertical channel are used to scrutinize closure assumptions for statistical modeling of bubble induced turbulence. The paper is closed by conclusions in section 5.

[1] Corresponding author

2. GOVERNING EQUATIONS AND NUMERICAL METHOD

2.1 Governing equations

We consider two immiscible Newtonian fluids with constant density and viscosity that are separated by a phase interface. The motion of each fluid is governed by the conservation equations of mass and momentum. At the interface the jump of normal stresses is balanced by surface tension. Here, we assume that the coefficient of surface tension is constant. Then, the governing equations can be written in the following non-dimensional single-field formulation:

$$\nabla \cdot \mathbf{u}_\mathrm{m} = 0 \tag{1}$$

$$\frac{\partial(\rho_\mathrm{m}\mathbf{u}_\mathrm{m})}{\partial t} + \nabla\cdot\rho_\mathrm{m}\mathbf{u}_\mathrm{m}\mathbf{u}_\mathrm{m} = -\nabla P + \frac{1}{Re_\mathrm{ref}}\nabla\cdot\mu_\mathrm{m}\left(\nabla\mathbf{u}_\mathrm{m} + (\nabla\mathbf{u}_\mathrm{m})^\mathrm{T}\right) - (1-f)\frac{Eo_\mathrm{ref}}{We_\mathrm{ref}}\mathbf{e}_\mathrm{g} + Eu_\mathrm{ref}\mathbf{e}_\mathrm{p} + \frac{a_\mathrm{in}\kappa\mathbf{n}_\mathrm{in}}{We_\mathrm{ref}} \tag{2}$$

The non-dimensional mixture density, center-of-mass velocity and mixture viscosity are defined by

$$\rho_\mathrm{m} \equiv \frac{f\rho_\mathrm{L}^* + (1-f)\rho_\mathrm{G}^*}{\rho_\mathrm{L}^*}, \quad \mathbf{u}_\mathrm{m} \equiv \frac{1}{U_\mathrm{ref}^*}\frac{f\rho_\mathrm{L}^*\mathbf{u}_\mathrm{L}^* + (1-f)\rho_\mathrm{G}^*\mathbf{u}_\mathrm{G}^*}{f\rho_\mathrm{L}^* + (1-f)\rho_\mathrm{G}^*}, \quad \mu_\mathrm{m} \equiv \frac{f\mu_\mathrm{L}^* + (1-f)\mu_\mathrm{G}^*}{\mu_\mathrm{L}^*} \tag{3}$$

where we use subscripts L and G to denote the (continuous) liquid and (disperse) gas phase, respectively, and use superscript * to indicate dimensional quantities. For normalization we use a reference length scale L_ref^* and a reference velocity scale U_ref^*.

In our simulations we will use periodic boundary conditions in one or two coordinate directions. The pressure field is, however, not periodic because of the hydrostatic contribution. To circumvent this problem we have introduced in Eq. (2) the "reduced pressure"

$$P \equiv \frac{1}{\rho_\mathrm{L}^* U_\mathrm{ref}^{*\,2}}\left(p^* - \rho_\mathrm{L}^*\mathbf{g}^*\cdot\mathbf{x}^* + \frac{|\Delta p^*|}{L_\mathrm{ref}^*}\mathbf{e}_\mathrm{p}\cdot\mathbf{x}^*\right) \tag{4}$$

Here, $|\Delta p^*|$ is the (constant) pressure drop in axial direction over the distance of the reference length. The present formulation of the pressure term implies that for mesh cells where $0 < f < 1$ we assume $p_\mathrm{L}^* = p_\mathrm{G}^* = p^*$. Due to the decomposition of Eq. (4) the influence of gravity is accounted for in the momentum Eq. (2) by the buoyancy force which involves the unit vector in direction of gravity, $\mathbf{e}_\mathrm{g}$. Similarly, a potentially imposed external pressure drop results in a body force term that involves the unit vector in axial direction, $\mathbf{e}_\mathrm{p}$. The last term in the mixture momentum equation (2) represents the surface tension force. There, $a_\mathrm{in} = a_\mathrm{in}^* L_\mathrm{ref}^*$ is the non-dimensional volumetric interfacial area concentration in the mesh cell, $\kappa = \kappa^* L_\mathrm{ref}^*$ is twice the non-dimensional mean curvature of the interface and $\mathbf{n}_\mathrm{in}$ is the unit normal vector to the interface pointing into the continuous phase, i.e. the liquid. The definitions of the reference Reynolds number (Re_ref), reference Eötvös number (Eo_ref), reference Weber number (We_ref) and reference Euler number (Eu_ref) appearing in Eq. (2) are

$$Re_\mathrm{ref} \equiv \frac{\rho_\mathrm{L}^* L_\mathrm{ref}^* U_\mathrm{ref}^*}{\mu_\mathrm{L}^*}, \quad Eo_\mathrm{ref} \equiv \frac{(\rho_\mathrm{L}^* - \rho_\mathrm{G}^*) g^* L_\mathrm{ref}^{*\,2}}{\sigma^*}, \quad We_\mathrm{ref} \equiv \frac{\rho_\mathrm{L}^* L_\mathrm{ref}^* U_\mathrm{ref}^{*\,2}}{\sigma^*}, \quad Eu_\mathrm{ref} \equiv \frac{|\Delta p^*|}{\rho_\mathrm{L}^* U_\mathrm{ref}^{*\,2}} \tag{5}$$

The set of equations is completed by the transport equation for the liquid volumetric fraction

$$\frac{\partial f}{\partial t} + \nabla \cdot f \mathbf{u}_{\mathrm{m}} = 0 \tag{6}$$

which expresses - in the absence of phase change - the mass conservation of the liquid phase. The derivation of the above set of equations is given in Wörner *et al.* (2001). Here, the equations are already in simplified form. Namely, it is assumed that within a mesh cell both phases move with the same velocity, i.e. the center-of-mass velocity $\mathbf{u}_{\mathrm{m}}$. This assumption corresponds to a locally homogeneous model.

2.2 Numerical method

We now give a short outline of the numerical method used in our in-house computer code TURBIT-VOF. The code is based on the finite volume method, uses Cartesian co-ordinates, and employs a regular staggered grid. The general solution strategy is based on a projection method where a conjugated gradient method is used to solve the resulting pressure Poisson equation. For approximation of spatial derivates a second order central difference scheme is used. The integration in time is done by a third order explicit Runge-Kutta method. The transport equation for the liquid volumetric fraction, Eq. (6), is solved by a volume of fluid method which involves two steps. First, for each mesh cell that instantaneously contains both phases, the interface orientation and location is reconstructed by the algorithm EPIRA (Exact Plane Interface Reconstruction Algorithm) that locally approximates the interface by a plane. In a second step the fluxes of liquid across the faces of the mesh cell are computed. For details about the numerical method we refer to Sabisch *et al.* (2001) and Ghidersa (2004).

3. BUBBLE TRAIN FLOW IN A SQUARE VERTICAL MINI-CHANNEL

3.1 Motivation

The prevailing trend to miniaturize conventional fluidic systems and devices for applications in chemical engineering has fostered recent interest in multiphase transport in small channels. Potential applications include miniaturized heat exchangers (Schubert *et al.*, 2001), evaporators, condensers, distillation units, liquid-liquid and gas-liquid reactors, monolithic catalyst reactors (Boger *et al.*, 2004), and multiphase extraction and separation units. For multiphase micro process engineering a large benefit stems from operating with gas and liquid layers of defined geometry with a defined interface, unlike most macroscopic disperse systems which typically have a size distribution of bubbles in the continuous liquid (Hessel *et al.*, 2004). Related to this, a further potential benefit is the operation in many parallel channels, each having the same two-phase flow pattern. For practical applications, this should allow for a favorable numbering up approach instead of scaling up.

The design and optimization of miniaturized devices require knowledge of the basic hydro-dynamical phenomena of the two-phase flow in a *single* channel. The typical two-phase flow pattern in narrow channels is known as bubble train flow. This term refers to the flow of a regular train of elongated bubbles (Taylor bubbles), having identical shape and distance from each other and moving with the same velocity. Bubble train flow is, therefore, fully described by a flow unit cell (UC).

The dominant forces for two phase flow in small channels are the viscous force and the surface tension force. The ratio between these two forces constitutes the capillary number

$$Ca_{\mathrm{B}} \equiv \frac{\mu_{\mathrm{L}}^{*} U_{\mathrm{B}}^{*}}{\sigma^{*}} \tag{7}$$

where U_B^* is the translational velocity of the bubble. Quantities of interest such as the bubble diameter D_B^* or the liquid film thickness are therefore usually correlated in terms of Ca_B. In the remainder of this chapter we summarize results of our recent numerical studies (Ghidersa *et al.* 2004, Wörner *et al.* 2004) of the co-current air-oil bubble train flow in a square vertical mini-channel of 2 mm width. In particular we discuss the bubble shape and flow structure for different values of the capillary number and analyze the influence of the length of the flow unit cell.

3.2 Simulation parameter

3.2.1 Fluid properties

One goal of our simulations is to investigate the influence of the capillary number. In the experiments of Thulasidas *et al.* (1995) e.g. a wide range of capillary numbers is realized by using silicon oil of different viscosity. Here, we adopt an equivalent procedure and perform simulations for two different values of the liquid viscosity. The viscosity of case A is about ten times lower than in case B. For the gas phase we use, unlike in Thulasidas *et al.* (1995) not air, but a gas with ten times higher density and viscosity, see Table 1. This is to increase the computational efficiency of our explicit time integration scheme, which results in severe time step restrictions in the case of very low density ratio (Wörner, 2002). This increase of the gas density is justified due to the results of the numerical study of Wörner (2003). In that paper the influence of the gas-liquid density ratio is investigated for the buoyancy driven rise of an oblate ellipsoidal bubble and a spherical cap bubble. It is found that under proper scaling the steady bubble shape and the velocity field inside the bubble and in the liquid are invariant with respect to a variation of the gas-liquid density ratio. In order to keep the ratio of the Reynolds numbers in the gas and liquid flow similar to the experiment, we increase the dynamic viscosity of the gas in the computations by a factor of 10, too. Therefore, the gas-liquid kinematic viscosity ratio is the same in the experiment and in our computations. The physical properties given in Table 1 result in a Morton number

$$M \equiv \frac{(\rho_L^* - \rho_G^*) g^* \mu_L^{*4}}{\rho_L^{*2} \sigma^{*3}} = 0.00493 \tag{8}$$

This value is only 1% lower than the value in the experiment of Thulasidas *et al.* (1995), where M = 0.00498.

Case	ρ_L^*	ρ_G^*	μ_L^*	μ_G^*	σ^*
A	913 kg/m^3	11.7 kg/m^3	0.0046 Pa s	1.84 $\times 10^{-4}$ Pa s	0.02218 N/m
B	957 kg/m^3	11.7 kg/m^3	0.048 Pa s	1.84 $\times 10^{-4}$ Pa s	0.02218 N/m

Table 1: Physical properties of liquid and gas used in the bubble train simulations for case A and B

In Table 2 we list the reference scales and the non-dimensional groups that appear in the mixture momentum equation. Note that the reference Euler number is estimated from the pressure drop of the single phase flow with the same liquid flow rate as in Thulasidas *et al.* (1995).

Case	L_{ref}^*	U_{ref}^*	Re_{ref}	Eo_{ref}	We_{ref}	Eu_{ref}
A	0.002 m	0.0626 m/s	24.85	1.59	0.323	0.2
B	0.002 m	0.0264 m/s	1.0527	1.67	0.060	27.03

Table 2: Reference scales and dimensionless numbers for the bubble train simulations

3.2.2 Computational grid

We consider the co-current upward directed bubble train flow in a square vertical channel with side length $W^* = 2$ mm. In our numerical simulation we model the flow unit cell by considering one bubble only and by using periodic boundary conditions in axial direction to account for the influence of the leading and trailing bubble. At the four side walls of the channel no-slip boundary conditions are imposed. We choose a Cartesian co-ordinate system with y^* as stream-wise vertical direction and x^* and z^* as horizontal wall-normal directions. Thus, the gravity vector points in negative y^* direction while $\mathbf{e}_p$ points in positive y^* direction. We normalize all length scales by $L_{ref}^* = W^* = 2$ mm so that the non-dimensional size of the computational box is $1 \times L_{uc} \times 1$. For the physical parameters of case A we perform only one simulation with a cubic flow unit cell, while for the physical parameters of case B we perform six simulation runs with five different values of L_{uc}, see Table 3. Thus, by the simulations for case B we investigate the influence of the length of the flow unit cell.

In all computations the grid is uniform. In case A1 and B1F it consists of cubic mesh cells of size $h = 1/64$. To investigate the influence of the grid simulation run B1C is performed with the same parameters as case B1F but a mesh size of $h = 1/48$. As will be shown below, the difference of the results is very small (see also Ghidersa *et al.*, 2004). This justifies the use of the coarser grid for the other runs of case B.

In all simulations the gas volumetric fraction in the flow unit cell is $\varepsilon = 33\%$. The initial bubble shape is spherical for cases A, B1F and B1C, and is an elongated body of revolution for the other cases (see Wörner *et al.*, 2004). All simulations are started from a quiescent state and several ten thousand time steps are computed. The non-dimensional time step width Δt corresponds to a Courant-Friedrichs-Levy number (based on the terminal bubble velocity) of about $CFL = U_B \, \Delta t / \Delta x \approx 0.02$ for case A and about 0.005 for case B.

Case	L_{uc}	computational domain	grid	Δt	time steps
A	1	$1 \times 1 \times 1$	$64 \times 64 \times 64$	1.0×10^{-4}	14,000
B1F	1	$1 \times 1 \times 1$	$64 \times 64 \times 64$	1.0×10^{-5}	60,000
B1C	1	$1 \times 1 \times 1$	$48 \times 48 \times 48$	2.5×10^{-5}	24,000
B2	1.25	$1 \times 1.25 \times 1$	$48 \times 60 \times 48$	2.5×10^{-5}	24,000
B3	1.5	$1 \times 1.5 \times 1$	$48 \times 72 \times 48$	2.5×10^{-5}	26,000
B4	1.75	$1 \times 1.75 \times 1$	$48 \times 84 \times 48$	2.5×10^{-5}	26,000
B5	2	$1 \times 2 \times 1$	$48 \times 96 \times 48$	2.5×10^{-5}	28,000

Table 3: Geometrical and computational parameters for the bubble train simulations

3.3 Results

3.3.1 Verification

In Table 4 the terminal values of the capillary number are given for the different simulations. For case A the capillary number has a value of 0.043 while for the simulations of case B the value of Ca_B is about five to six times higher. Table 4 also lists the values of the non-dimensional diameter, $D_B = D_B^* / L_{ref}^*$, of the bubble in the cross-section where the liquid film thickness is smallest. The bubble diameter is computed as follows. First, for each mesh cell $f_{i,j,k}$ that contains both phases ($0 < f_{i,j,k} < 1$) the centroid of the plane representing the phase interface is computed. The centroid of neighboring mesh cells are then connected to form triangles or quadrangles. This yields a closed surface (see Fig. 2). By this procedure it is possible to determine the bubble dimensions with a resolution that is smaller than the actual mesh width h. Also given in Table 4 are values of the ratio of bubble velocity and mean velocity in the liquid slug, $V \equiv U_B^* / U_{sl}^*$ and for the relative bubble velocity $Z \equiv (U_B^* - U_{sl}^*) / U_B^*$.

To validate our simulations we compare the computed values for D_B, V and Z with the respective experimental data of Thulasidas *et al.* (1995), who display their results in graphical form as function of Ca_B. For case A the computed values for V and Z given in Table 4 agree very well with the experimental data. However, the computed value of D_B is slightly too low. In the simulations for case B the range of the capillary number is $0.204 \leq Ca_B \leq 0.253$. For this range Thulasidas *et al.* (1995) give values falling (with some scattering) in the range $0.82 < D_B < 0.86$, $1.68 < V < 1.84$ and $0.435 < Z < 0.475$, respectively. Thus, our computational results for V and Z listed in Table 4 do well agree with these experimental data. For the bubble diameter we obtain good agreement for simulations B2, B3 and B4, where $L_{uc} \geq 1.25$ while for runs B1F and B1C the computed value of D_B is somewhat too small. The reason for this discrepancy will be discussed in section 3.3.4. For information we also list in Table 4 the terminal values of the bubble Reynolds number $Re_B \equiv \rho_L^* D_B^* U_B^* / \mu_L^*$.

Case	L_{uc}	Ca_B	D_B	V	Z	Re_B
A	1	0.043	0.92	1.55	0.355	82.87
B1F	1	0.205	0.81	1.80	0.446	3.80
B1C	1	0.206	0.81	1.80	0.445	3.79
B2	1.25	0.207	0.84	1.75	0.430	3.80
B3	1.5	0.219	0.85	1.75	0.430	4.03
B4	1.75	0.238	0.85	1.78	0.438	4.39
B5	2	0.257	0.85	1.80	0.445	4.74

Table 4: Results for the different bubble train simulations

3.3.2 Bubble shape

We now discuss the bubble shape for the different bubble train simulations. The generally accepted minimum value of the capillary number for which the bubble shape in a square channel remains axisymmetric (i.e. the bubble cross-section at any axial position is circular) is $Ca_{axi} = 0.04$ (Ratulowski & Chang, 1989; Thulasidas *et al.*, 1995). The smallest value of the capillary number in our simulations is obtained for case A, where $Ca_B = 0.043$. Indeed, for this case and all the other cases the computed bubble shape is axisymmetric.

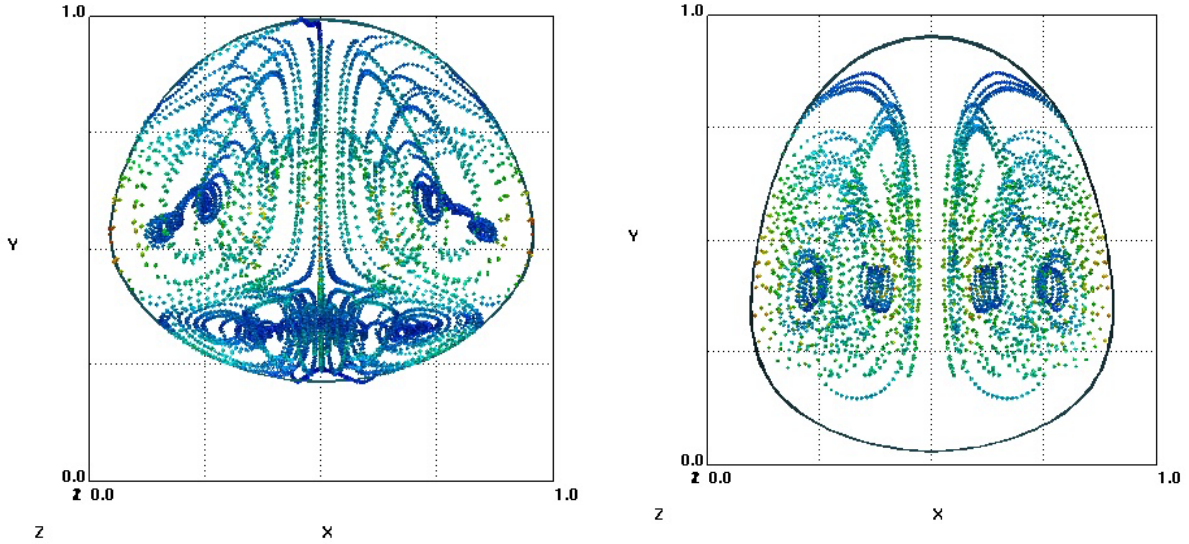

Figure 1: Bubble shape and flow structure within the bubble for case A (left) and case B1F (right).

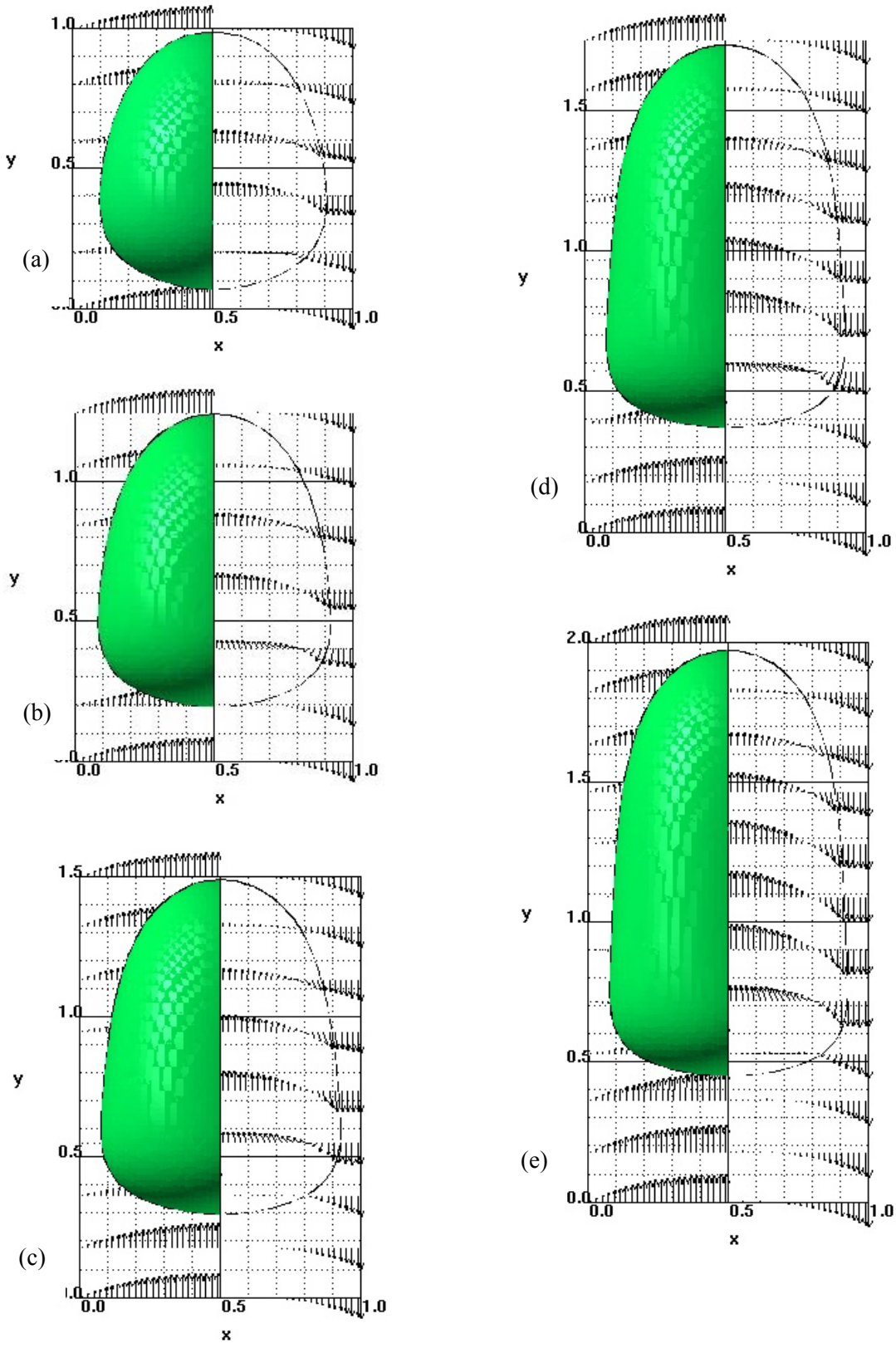

Figure 2: Bubble shape and velocity field in vertical mid-plane for fixed frame of reference (left half) and for frame of reference linked to the bubble (right half) for (a): case B1C, (b): case B2, (c): case B3, (d): case B4, (e): case B5. In *y*-direction only every 8th vector is displayed.

Figure 1 compares the computed steady bubble shape in a vertical mid-plane for case A and B1F. We see that for case A the bubble shape is close to spherical while in case B it is rather elongated. Accordingly, for case A the thickness of the liquid film is much smaller than for case B1F. Also shown in Fig. 1 is a visualization of the flow structure within the bubble for a referential system moving with the bubble. This visualization is obtained by inserting mass-less particles at different positions inside the bubble and observing their advection by the velocity field. For case B1F the flow inside the bubble forms a single toroidal vortex, while in case A a second vortex appears at the rear of the bubble. The latter vortex is driven by a counter-rotating vortex inside the liquid slug, see Ghidersa *et al.* (2004) for a detailed discussion.

Figure 2 shows the left half of the steady bubble shape for the simulations B1C, B2, B3, B4 and B5. To allow for a good visualization for each case the results are given for an instant in time when the bubble tip is almost at the top of the computational domain. A detailed comparison of the bubble shape shows that the radius of curvature of the bubble tip, r_{tip}, is almost the same for case B1C and B2. Also for case B3, B4 and B5 the value of r_{tip} is about the same, but is somewhat smaller than for case B1C and B2. The radius of curvature at the bubbles rear is a little bit smaller for case B1C than for case B2, both being smaller than those of case B3, B4 and B5 which is almost the same for these three cases.

3.3.3 Velocity field

Figure 2 additionally shows the velocity field in the axial mid-plane for five different simulations of case B. In the left half of the figure the velocity field is shown for a fixed frame of reference while in the right half it is displayed for the frame of reference moving with the bubble, i.e. the bubble velocity is subtracted from the vertical velocity component. We begin our discussion with the velocity field in the fixed frame of reference. The velocity profile in the liquid slug has the form of a parabola and is similar for all five cases. In the region where the liquid film is very thin the liquid velocity is almost zero. In the frame of reference moving with the bubble the flow inside the bubble can be analyzed. We find that there is one big vortex which occupies almost the complete bubble. In the rear part of the bubble, however, the velocity is almost zero in the frame of reference moving with the bubble. As regards to the flow in the liquid, the velocity profiles in this frame of reference indicate that part of the liquid slug that is moving with the velocity of the bubble.

3.3.4 Capillary number dependence of the bubble diameter

We now discuss for the simulations of case B the dependence of the bubble diameter on the capillary number. The results displayed in Figure 3 show that there is first an increase of D_B with Ca_B (cases B1C, B2, B3) but then there is a decrease (cases B3, B4 and B5). This result is in contrast to the experimental study of Thulasidas *et al.* (1995) who find a monotonic decrease of the bubble diameter with increasing capillary number. We interpret this finding as follows: in the experiments of Thulasidas *et al.* (1995) the bubble length is always larger than the width of the channel, while in our simulations this is not the case and the ratio $L_B = L_B^* / W^*$ ranges from 0.93 in case B1C to 1.53 for case B5 (see Wörner *et al.*, 2004). In Figure 3 we also show the variation of L_B with Ca_B. The data suggest that there may exist a critical bubble length $L_{B,crit} \approx 1.2$. For values smaller than $L_{B,crit}$ the bubble diameter increases with increasing capillary number while for values larger than $L_{B,crit}$ it decreases. However, the accurate determination of $L_{B,crit}$ requires further simulations especially in the range $1.25 < L_{uc} < 1.75$. While the computational results for D_B over Ca_B in Fig. 3 show a local maximum, we find for the dependence of V and Z on L_{uc} and Ca_B a local minimum (Wörner *et al.*, 2004). These results suggest that there is a significant change in the flow conditions when the bubble length exceeds $L_{B,crit}$.

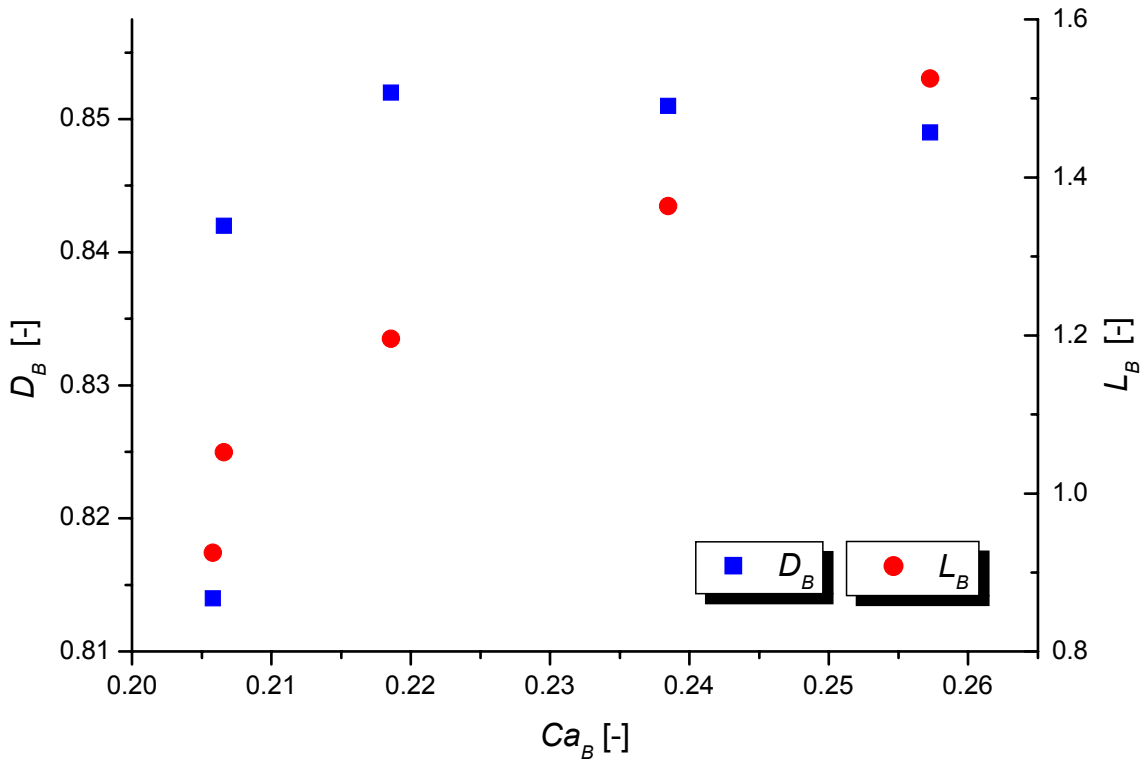

Figure 3: Non-dimensional bubble diameter and bubble length as function of the capillary number for the bubble train simulations of case B.

4. ANALYSIS OF LIQUID PHASE TURBULENCE KINETIC ENERGY EQUATION FOR BUBBLE SWARM FLOW

4.1 Motivation

While modelling of turbulent single phase flows has already reached a certain level of maturity, models for the turbulence in bubbly flows are still under development. Most of the difficulties faced in the development of advanced turbulence models for bubbly flows concern the pure understanding of mechanisms in which bubbles alter generation, dissipation and redistribution of turbulence kinetic energy in the liquid phase. Analytically, these mechanisms were formulated by the derivation of the balance equation for liquid turbulence kinetic energy in gas-liquid flows (Kataoka & Serizawa, 1989). Although known for more than a decade this equation could not be exposed to an appropriate quantitative analysis, because highly resolved data on the flow field and phase interface structure required for such an analysis have not been available.

In this chapter we use DNS data of the rise of a bubble swarm in a vertical channel through an otherwise stagnant liquid to scrutinize closure assumptions for statistical modelling of bubble-induced turbulence (BIT). The cornerstone of many models is given by the transport equation for turbulence kinetic energy within the liquid phase, k_L. Here, we evaluate the different terms in the analytical form of this equation from our DNS data and obtain by this way the budget of k_L. Furthermore, we analyse the performance of models proposed in literature for the closure of so called interfacial term in the k_L-equation. A similar analysis has already been performed for bubble train flow (Ilić *et al.*, 2004).

4.2 Computational set-up

The modeling of BIT is of special importance for situations where the only force driving the flow is given by buoyancy. An example of such a flow is encountered in bubble columns which are widely used in chemical engineering. For investigation of such flows in a laboratory often flat bubble columns are used. In such a flat tank filled with an otherwise stagnant liquid, bubbles are injected at the bottom. The bubbles rise in the central part of the bubble column and induce a re-circulatory motion of the liquid, see Figure 4. Because there is no net upward liquid flow, the liquid flows downward close to the four side walls.

In our simulations we want to mimic the situation in a flat bubble column. Because of limited computer resources we can, however, not consider the entire tank with thousands of bubbles. Instead we consider only a small part of the flat bubble column. Namely, our computational domain consists of two rigid side walls while in the vertical and span-wise direction we use periodic boundary conditions. The non-dimensional size of this domain is $1 \times 1 \times 1$ and it is discretized by 64^3 uniform mesh cells. The reference length is $L_{\mathrm{ref}}^{*} = 4$ m and the reference velocity is $U_{\mathrm{ref}}^{*} = 1$ m/s. In the computational box eight spherical bubbles with non-dimensional diameter $d_{\mathrm{B}} \equiv d_{\mathrm{B}}^{*} / L_{\mathrm{ref}}^{*} = 0.25$ are placed, see Figure 5. This corresponds to an overall gas content of $\varepsilon = 6.5$ %. The value of the gas-liquid density ratio is 0.5, that of the gas-liquid viscosity ratio is 1, the Morton number is 3.06×10^{-6} and the bubble Eötvös number is $Eo_{\mathrm{B}} \equiv (\rho_{\mathrm{L}}^{*} - \rho_{\mathrm{G}}^{*}) g^{*} d_{\mathrm{B}}^{*2} / \sigma^{*} = 3.065$. The values of the reference input numbers are $Re_{\mathrm{ref}} = 100$, $Eo_{\mathrm{ref}} = 49.05$, $Eu_{\mathrm{ref}} = 0$ and $We_{\mathrm{ref}} = 2.5$. The simulation is started from stagnant conditions. In total about 60,000 time steps with a time step width $\Delta t = 0.5 \times 10^{-4}$ are computed. We note that to obtain a down-flow of the liquid phase close to the walls, we have introduced an additional body force in the momentum equation. Therefore, the buoyancy term in momentum equation (2) is replaced by

$$-(1 - f - \varepsilon) \frac{Eo_{\mathrm{ref}}}{We_{\mathrm{ref}}} \mathbf{e}_{\mathrm{g}} \tag{9}$$

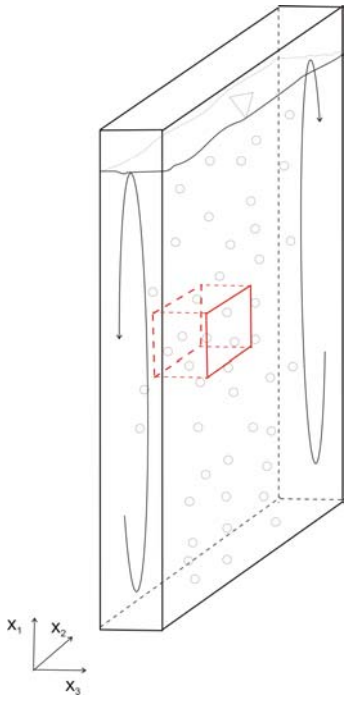

Figure 4: Sketch of flow in a flat bubble column. The small red box illustrates the computational domain.

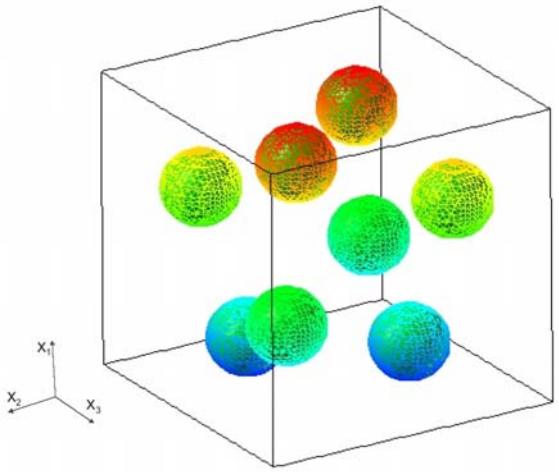

Figure 5: Initial configuration of bubble swarm simulation.

4.3 Liquid phase turbulence kinetic energy equation

For an incompressible liquid phase the non-dimensional specific turbulent kinetic is given by

$$k_{\mathrm{L}} \equiv \frac{1}{2}\overline{\overline{\mathbf{u}_{\mathrm{L}}^{'} \cdot \mathbf{u}_{\mathrm{L}}^{'}}} = \frac{1}{2}\frac{1}{U_{\mathrm{ref}}^{*\,2}}\overline{\overline{\mathbf{u}_{\mathrm{L}}^{*\prime} \cdot \mathbf{u}_{\mathrm{L}}^{*\prime}}} \tag{10}$$

The transport equation for k_{L} has been derived by Kataoka and Serizawa (1989). With the normalization used in the present paper, it translates in the following non-dimensional form

$$\begin{aligned}\frac{\partial}{\partial t}(\alpha_{\mathrm{L}} k_{\mathrm{L}}) + \nabla\cdot\left(\alpha_{\mathrm{L}} k_{\mathrm{L}} \overline{\mathbf{u}_{\mathrm{L}}}\right) = \underbrace{\frac{1}{Re_{\mathrm{ref}}}\nabla\cdot\left(\alpha_{\mathrm{L}}\overline{\overline{\mathrm{T}_{\mathrm{L}}^{'}\cdot\mathbf{u}_{\mathrm{L}}^{'}}}\right) - \nabla\cdot\left[\alpha_{\mathrm{L}}\left(\overline{\overline{p_{\mathrm{L}}^{'}\mathbf{u}_{\mathrm{L}}^{'}}} + \frac{1}{2}\overline{\overline{(\mathbf{u}_{\mathrm{L}}^{'}\cdot\mathbf{u}_{\mathrm{L}}^{'})\mathbf{u}_{\mathrm{L}}^{'}}}\right)\right]}_{DIFFUSION} \\ \underbrace{-\alpha_{\mathrm{L}}\overline{\overline{\mathbf{u}_{\mathrm{L}}^{'}\mathbf{u}_{\mathrm{L}}^{'}}} : \nabla\overline{\mathbf{u}_{\mathrm{L}}}}_{PRODUCTION} \underbrace{-\frac{1}{Re_{\mathrm{ref}}}\alpha_{\mathrm{L}}\overline{\overline{\mathrm{T}_{\mathrm{L}}^{'}:\nabla\mathbf{u}_{\mathrm{L}}^{'}}}}_{DISSIPATION} + \underbrace{\overline{\left[\frac{1}{Re_{\mathrm{ref}}}\mathrm{T}_{\mathrm{L;in}}^{'} - p_{\mathrm{L;in}}^{'}\mathrm{I}\right]\cdot\mathbf{u}_{\mathrm{L;in}}^{'}\cdot\mathbf{n}_{\mathrm{L;in}}a_{\mathrm{in}}}}_{INTERFACIAL\ TERM}\end{aligned} \tag{11}$$

where the non-dimensional fluctuating viscous stress tensor of the liquid phase is given by

$$\mathrm{T}_{\mathrm{L}}^{'} = \mu_{\mathrm{L}}\left[\nabla\mathbf{u}_{\mathrm{L}}^{'} + (\nabla\mathbf{u}_{\mathrm{L}}^{'})^{\mathrm{T}}\right] \tag{12}$$

The following notation is used. Subscript 'L;in' denotes liquid phase quantities at the gas-liquid interface and α_{L} is the mean liquid volumetric fraction defined as

$$\alpha_{\mathrm{L}} \equiv \overline{X_{\mathrm{L}}}\,, \tag{13}$$

where $X_{\mathrm{L}}(\mathbf{x},t)$ is the characteristic function of the liquid phase, which is unity if point $\mathbf{x}$ is within the liquid at time t and is zero otherwise. The single overbar $\overline{\ }$ indicates averaging and the double overbar $\overline{\overline{\ }}$ denotes so-called phase-weighted averaging. For an arbitrary physical quantity of the liquid phase, A_L, this averaging is defined as

$$\overline{\overline{A_{\mathrm{L}}}} \equiv \frac{\overline{A_{\mathrm{L}}X_{\mathrm{L}}}}{\overline{X_{\mathrm{L}}}} = \frac{\overline{A_{\mathrm{L}}X_{\mathrm{L}}}}{\alpha_{\mathrm{L}}} \tag{14}$$

Fluctuating parts of physical quantities are evaluated as

$$A_{\mathrm{L}}^{'} \equiv A_{\mathrm{L}} - \overline{\overline{A_{\mathrm{L}}}} \quad \text{and} \quad A_{\mathrm{L;in}}^{'} \equiv A_{\mathrm{L;in}} - \overline{\overline{A_{\mathrm{L}}}} \tag{15}$$

On the left-hand-side of Eq. (11) we have the unsteady and convective transport term. On the right-hand-side of Eq. (11) two distinctive groups of terms appear. The first one is the group of terms associated with the mean liquid volumetric fraction, α_L. Except for being multiplied with α_L, these terms are basically of the same form as the ones involved in the single-phase turbulence kinetic energy equation, i.e. the diffusion, production and dissipation term can be recognized. For this reason these terms are called single-phase-like terms. The last term, that is associated with the interfacial area concentration a_{in}, represents a source of liquid turbulence attributed to the presence of bubble interfaces and is called interfacial term. Derivation of equation (11) is based on the local instant formulation of the mass and momentum conservation laws for two-phase flow, i.e. no model assumptions are made. In this context, Eq. (11) is called 'exact' k_{L} equation in order to distinguish it from the modelled k_{L} equation employed in turbulence models.

To evaluate the individual terms in Eq. (11) we replace the phase indicator function X_L by its discrete counter-part, the liquid volumetric fraction $f_{i,j,k}$ in a mesh cell. For the averaging procedure we take advantage from the fact that in our simulation we use periodic boundary conditions in vertical and stream-wise direction. Thus, both directions can be considered as homogeneous, so that statistical quantities will not depend on x_1 and x_2 but only on the wall-normal direction x_3. Assuming an equidistant grid we therefore adopt the following plane averaging procedure

$$\overline{A_{\mathrm{L};k}} = \frac{1}{N_1 N_2} \sum_{i=1}^{N_1} \sum_{j=1}^{N_2} f_{i,j,k} A_{\mathrm{L};i,j,k} \qquad \text{and} \qquad \overline{\overline{A_{\mathrm{L};k}}} = \frac{\sum_{i=1}^{N_1} \sum_{j=1}^{N_2} f_{i,j,k} A_{\mathrm{L};i,j,k}}{\sum_{i=1}^{N_1} \sum_{j=1}^{N_2} f_{i,j,k}} \tag{16}$$

where $k = 1,...,N_3$ and N_1, N_2 and N_3 represent the number of mesh cells in x_1 (i) , x_2 (j) and x_3 (k) direction, respectively.

The evaluation of the interfacial term in Eq. (11) requires knowledge of the pressure and velocity on the liquid side of the interface. The procedure adopted to compute these quantities is described in Ilić *et al.* (2004) and will not be repeated here.

The plane averaging procedure described above applies to a certain instant in time. We carry out this procedure for a number of instants in time (typically 40) for which DNS data have been stored on disk. The profiles obtained for the different instants in time are then linearly averaged. As only time levels that represent statistically fully developed flow are used, the unsteady term in Eq. (11) should be close to zero.

4.3 Results

4.3.1 Bubble shape

To give an overall impression of the flow structure we show in Figure 6 the shape and distribution of the bubbles for a certain instant in time from a lateral side and from top. Additionally shown is the velocity field in a certain plane. The bubbles have a shape that is close to an axisymmetric ellipsoid. The major axis of the bubbles is nearly horizontal, but does not exactly lie within a horizontal plane. Although some differences in the shape of individual bubbles can be observed, these are in general small and the average ratio of the major to the minor axis of the ellipsoidal bubbles is about 1.52.

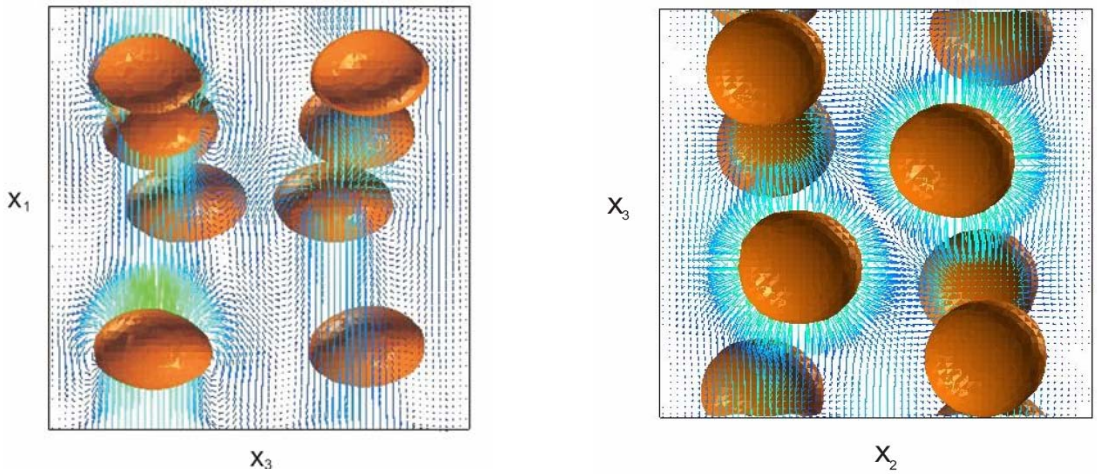

Figure 6: Visualization of bubble swarm flow. Lateral view with velocity field in plane $x_2 = 0.78$ (left) and view from top with velocity field in plane $x_1 = 0.59$ (right).

4.3.2 Profiles of mean quantities

In Figure 7 we show wall-normal profiles of certain plane averaged non-dimensional mean quantities. The marker-less red solid line represents the mean gas volumetric fraction $\alpha_G \equiv 1 - \alpha_L$. The profile is saddle type with α_G being zero close to the walls and small in the central part of the channel. The two maxima are located at a distance from the wall which is about 25% of the channel width. This profile is consistent with the bubble distribution shown in Figure 6. The profile of the mean vertical liquid velocity shows that the liquid flows upward where α_G is large but flows downward close to both walls and in the middle of the channel. The mean vertical gas velocity is positive (i.e. upward directed) almost every where and its maximum value is about 2.8 times higher than that of the liquid. The wall-normal profile of the non-dimensional liquid turbulent kinetic energy is zero close to the walls and shows a plateau with some variations in the center of the channel.

4.3.3 Balance of exact k_L equation

In Figure 8 we show wall-normal profiles of the balance terms on the right-hand-side of Eq. (11). Note that due to the plane averaging procedure adopted here, the convective term on the left-hand-side of Eq. (11) is zero. We also do not evaluate the unsteady term. Its order of magnitude can be estimated from the sum of the terms on the right-hand-side of Eq. (11). The 'out-of-balance' profile in Figure 8 shows that the unsteady term is close to zero and the flow is therefore statistically fully developed.

We start our discussion of the budget of k_L with the production term. In single phase flow this term is the only source term in the k_L-equation. It is related to the shear of the mean velocity field. From Figure 8 we see that for the present bubble swarm flow the production term is almost zero. The main source of k_L is due to the interfacial term while the main sink is due to the dissipation term. Both terms are large where α_G is large. However, the interfacial term and the dissipation term are not in local equilibrium. As a consequence the diffusion term redistributes turbulence kinetic energy from regions of high α_G to regions of low α_G.

4.3.4 Modeling of the interfacial term

The budget of the liquid phase turbulence kinetic energy has shown that for bubble driven flows – in the absence of a significant mean shear rate – the interfacial term is the only source term in the k_L equation. In engineering CFD computations the interfacial term must be modeled to close the k_L equation. The reliable modeling of this term is therefore of paramount importance for bubble driven flows. In Table 5 five different models for closure of the interfacial term are presented. It is generally assumed that bubbly flows are drag dominated. Namely, as it can be seen in Table 5, the work of the drag force, W_D^*, is included in all models, while in models 2, 3 and 5 it is even the only contribution. The evaluation of W_D^* is in models 2–5 based on the mean relative velocity, but in model 1 the terminal velocity U_T^* of a single bubble is used. The drag coefficient in models 1–4 is evaluated as

$$C_D = \frac{2}{3} Eo_B^{0.5} \left\{ \frac{1+17.67\alpha_L^{1.3}}{18.67\alpha_L^{1.5}} \right\}^2 , \tag{17}$$

while the constant value $C_D = 0.44$ is used in model 5. Van Driest's function, f_w, used in model 1 is formulated in the same way as in single phase flows. For the definition of the coefficient C_t see Hill *et al.* (1995). Non-drag contributions, W_{ND}^*, are in model 1 included through an additional term that accounts for absorption of liquid phase turbulence by bubbles, while in model 4 the work of the added-mass force is considered.

177ème Session du comité scientifique et technique de la Société Hydrotechnique de France
Progrès récents des méthodologies de modélisation des écoulements diphasiques, Lyon, France, 24-26 novembre 2004.
Advances in the modelling methodologies of two-phase flows, Lyons, France, November 24-26, 2004.

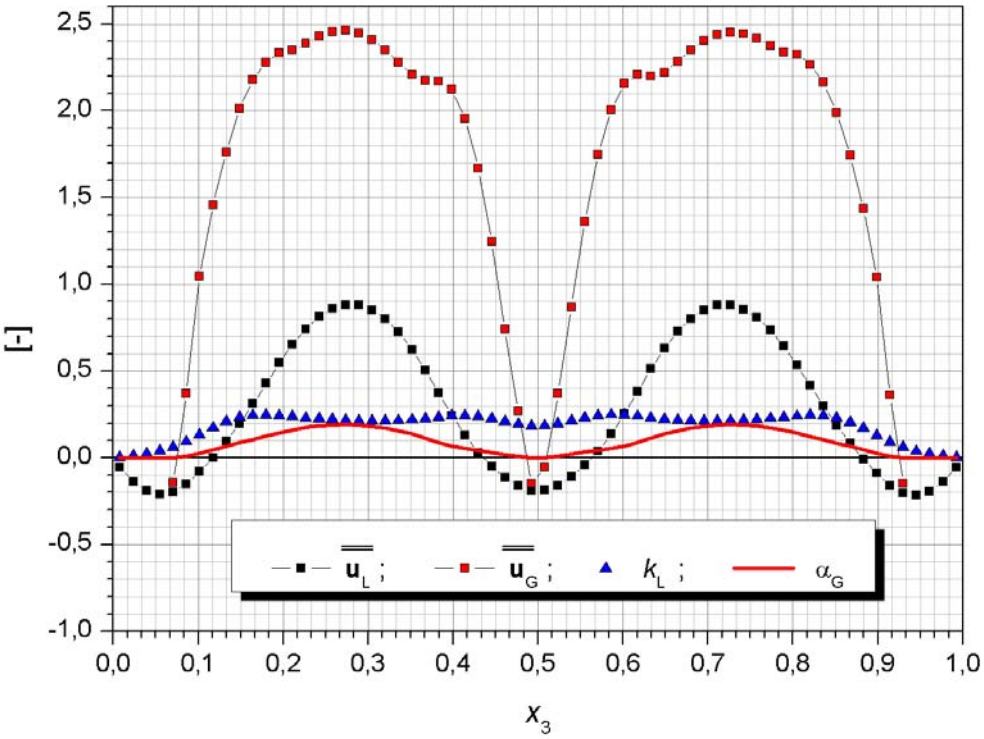

Figure 7: Wall-normal profiles of plane averaged non-dimensional mean quantities.

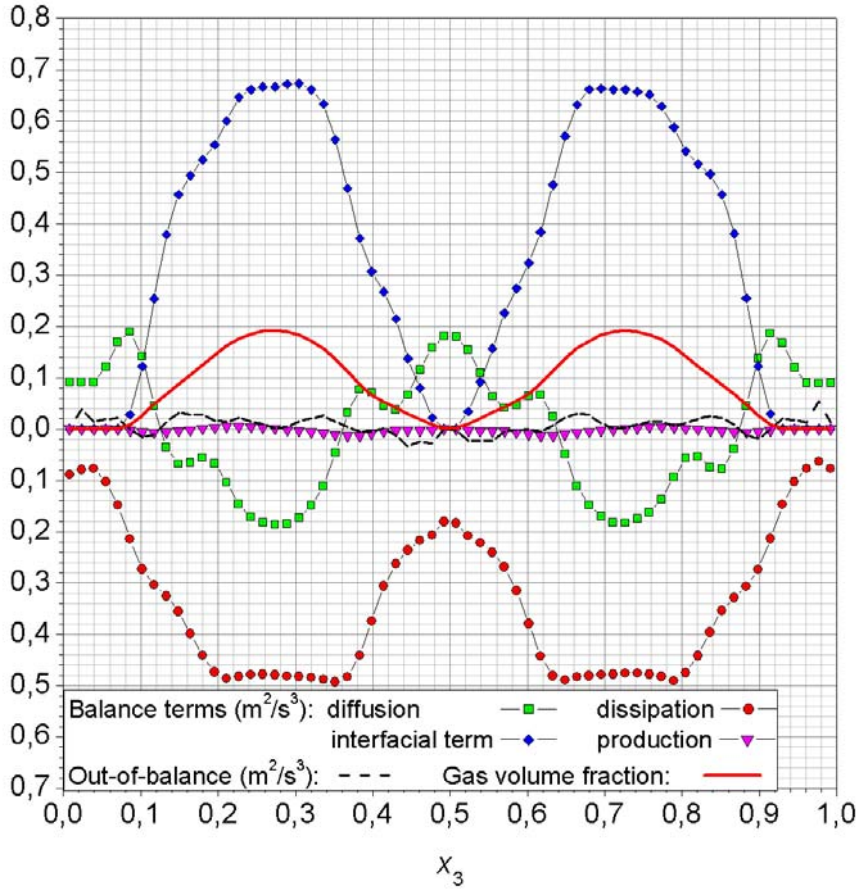

Figure 8: Wall-normal profiles of balance terms in liquid phase turbulence kinetic energy equation.

Reference	Work of drag force, W_D^*	Other contributions, W_{ND}^*
Kataoka & Serizawa (1997) Model 1, KS	$0.075 f_w \left[\frac{3}{4} \alpha_G \frac{C_D}{d_B^*} U_T^{*3} \right]$	$-\alpha_G \frac{k_L^{*3/2}}{d_B^*}$
Hill *et al.* (1995) Model 2, HWGI	$\frac{3}{4} \frac{\alpha_G C_D}{d_B^*} \left\| \overline{\mathbf{u}}_R^* \right\| \left\{ \frac{\mu_L^* \overline{\mathbf{u}}_R^* \cdot \nabla^* \alpha_G}{0.3 \rho_L^* \alpha_L \alpha_G} + 2k_L^* (C_t - 1) \right\}$	None
Lahey & Drew (2000) Model 3, LD	$\frac{1}{4} \alpha_L \left(1 + C_D^{4/3}\right) \alpha_G \frac{\left\| \overline{\mathbf{u}}_R^* \right\|^3}{d_B^*}$	None
Morel (1997) Model 4, M	$\frac{3}{4} \alpha_G \frac{C_D}{d_B^*} \left\| \overline{\mathbf{u}}_R^* \right\|^3$	$\frac{1+2\alpha_G}{2\alpha_L} \alpha_G \left\{ \frac{D_G \overline{\mathbf{u}}_G^*}{Dt^*} - \frac{D_L \overline{\mathbf{u}}_L^*}{Dt^*} \right\} \cdot \overline{\mathbf{u}}_R^*$
Pfleger & Becker (2001) Model 5, PB	$1.44 \alpha_L \left[\frac{3}{4} \alpha_G \frac{C_D}{d_B^*} \left\| \overline{\mathbf{u}}_R^* \right\|^3 \right]$	None

Table 5: Closure assumptions for (dimensional) interfacial term in modeled k_L^*-equation

In Figure 9 we compare the predictions of the models listed in Table 5 with the exact interfacial term as evaluated from our DNS data and thus make an 'a priori' test of the models. We see that model 4 (M) performs best, though it somewhat overestimates the interfacial term. All other models underestimate the magnitude of the interfacial term. Comparison of the profiles for model 4 (M) and model 5 (PB) reveals the importance of the proper choice of the drag coefficient C_D. Namely, although the 'standard' definition of the work of the drag force used in model 4 is in model 5 multiplied with $1.44\alpha_L$ (an expression that is here greater than 1), due to the inappropriate value of $C_D = 0.44$ (valid for particulate Reynolds number higher than 1000) this model underestimates the interfacial term. Since the terminal bubble velocity is of the same order of magnitude as the mean relative velocity, the underestimation of the interfacial term by the model 1 can be attributed to the factor $0.075 f_w$.

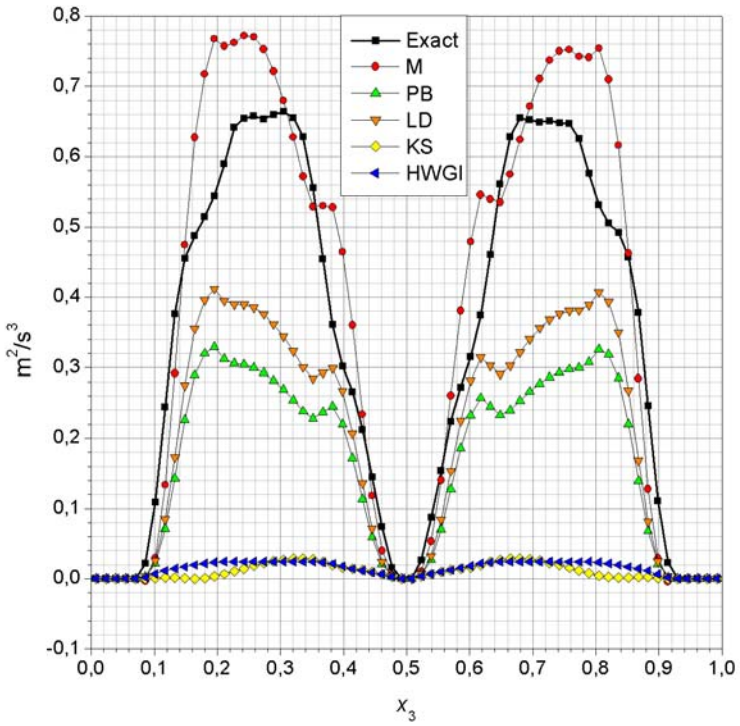

Figure 9: Wall-normal profiles of interfacial term. Comparison of the predictions by the models listed in Table 5 with exact term evaluated from DNS data.

5. CONCLUSIONS

In the first part of the paper direct numerical simulations of the co-current bubble train flow in a square vertical mini-channel have been presented. The focus was to study the influence of the capillary number and the influence of the length of the flow unit cell. For the dependence of the bubble diameter on the capillary number the new result was obtained that there is a regime where the bubble diameter increases with the capillary number and another regime where it decreases with increasing capillary number. It appears that the criterion determining the transition between both regimes is related to a critical ratio of bubble length to channel width of about 1.2.

The second part of the present paper has dealt with the quantitative analysis of the balance equation for the liquid phase turbulence kinetic energy in gas-liquid bubbly flows. To provide the data for the analysis, simulations of a swarm of eight ellipsoidal bubbles rising through an initially stagnant liquid within a narrow plane vertical channel are performed. The analysis of the budget of the turbulence kinetic energy equation for the liquid phase reveals the importance of the interfacial term which is the only source of turbulence kinetic energy. Models proposed in literature for closure of the interfacial term have been analyzed and critically evaluated.

NOMENCLATURE

a_{in}	non-dimensional interfacial area concentration	-	
C_D	drag coefficient	-	
Ca_B	capillary number	-	Eq. (7)
D_B^*	largest diameter of Taylor bubble	m	
d_B^*	equivalent bubble diameter	m	
$\mathbf{e}_g$	unit vector in direction of gravity	-	
$\mathbf{e}_p$	unit vector in direction of axial pressure drop	-	
Eo_{ref}	reference Eötvös number	-	Eq. (5)
Eu_{ref}	reference Euler number	-	Eq. (5)
f	liquid volumetric fraction within a mesh cell	-	
g^*	gravitational acceleration	$m^2\ s^{-1}$	
$\mathbf{g}^*$	gravity vector	$m^2\ s^{-1}$	
h	non-dimensional mesh width	-	
I	unit tensor	-	
k_L	non-dimensional liquid phase turbulence kinetic energy	-	
L_{ref}^*	reference length	m	
N_1, N_2, N_3	number of mesh cells	-	
$\mathbf{n}_{in}$	unit normal vector to interface pointing in continuous phase	-	
p^*	pressure	Pa	
P	reduced pressure	-	Eq. (4)
Re_{ref}	reference Reynolds number	-	Eq. (5)

t^*	time	s
U_B^*	bubble velocity	m s^{-1}
U_{ref}^*	reference velocity	m s^{-1}
$\mathbf{u}$	velocity field	-
V	ratio between bubble velocity and slug velocity	-
W^*	channel width	m
W_D^*, W_{ND}^*	work of drag force and non-drag forces	J
We_{ref}	reference Weber number	-
X_L	phase indicator function of liquid phase	-
$\mathbf{x}$	position vector, $\mathbf{x} = (x, y, z)$ or $\mathbf{x} = (x_1, x_2, x_3)$	-
Z	relative bubble velocity	-

Greek symbols

α	local mean volumetric fraction	-
ε	overall gas holdup in computational domain	-
κ^*	interface curvature	m^{-1}
ρ^*	density	kg m^{-3}
μ^*	dynamic viscosity	Pa s
σ^*	coefficient of surface tension	N m^{-1}

Subscripts

B	bubble
crit	critical value
G	gas phase
in	interface
L	liquid phase
m	mixture quantity
R	relative
sl	slug
uc	unit cell

Superscripts

*	dimensional quantity

REFERENCES

Boger, T., Heibel, A.K., Sorensen C.M., 2004. Monolithic catalysts for the chemical industry. *Ind. Eng. Chem. Res.* **43**, 4602-4611.

Ghidersa, B.E., 2004. Finite-volume-based volume-of-fluid method for the simulation of two-phase flow in small rectangular channels. Forschungszentrum Karlsruhe, Wissenschaftliche Berichte, FZKA 6889 (http://bibliothek.fzk.de/zb/berichte/FZKA6889.pdf).

Ghidersa, B.E., Wörner, M., Cacuci, D.G., 2004. Exploring the flow of immiscible fluids in a square vertical mini-channel by direct numerical simulation. *Chem. Eng. J.* **101**, 285-294.

Hessel, V., Hardt, S., Löwe, H., 2004. *Chemical micro process engineering*. Wiley, Weinheim.

Hill, D. P., Wang, D. M., Gosman, A. D., Issa, R. I., 1995. Numerical predictions of two-phase bubbly flow in a pipe. Proc. 2nd Int. Conf. on Multiphase Flow, Kyoto, Japan, MO3-1 – MO3-6.

Hirt, C.W., Nichols, B.D., 1981. Volume of Fluid (VoF) method for the dynamics of free boundaries. *J. Comput. Phys*. **39**, 201-225.

Ilić, M., Wörner, M., Cacuci, D.G., 2004. Balance of liquid-phase turbulence kinetic energy equation for bubble train flow. *J. Nuclear Science Techn.* **41**, 331-338.

Kataoka, I., Serizawa, A., 1989. Basic equations of turbulence in gas-liquid two-phase flows. *Int. J. Multiphase Flow* **15**, 843-855.

Kataoka, I., Serizawa, A., 1997. Turbulence characteristics and their application to multi-dimensional analysis of two-phase flow. Proc. 8th International Topical Meeting on Nuclear Reactor Thermal-Hydraulics, Kyoto, Japan, Vol. 3, 1677-1683.

Lahey Jr., R.T., Drew, D., 2000. An analysis of two-phase flow and heat transfer using a multidimensional, multi-field, two-fluid computational fluid dynamics (CFD) model. Proc. Japan/US Seminar on Two-phase Flow Dynamics, June 5-8, 2000, Santa Barbara, USA.

Morel, C., 1997. Turbulence modelling and first numerical simulations in turbulent two-phase flows. Proc. 11th Symp. on Turbulent Shear Flows, Grenoble, France, p. P3.10 – P3.15.

Pfleger, D., Becker, S., 2001. Modelling and simulation of the dynamic flow behaviour in a bubble column. *Chem. Eng. Sci*. **56**, 1737-1747.

Ratulowski J., Chang H.-C., 1989. Transport of gas bubbles in capillaries. *Phys. Fluids* A **1**, 1642-1655.

Sabisch, W., Wörner, M., Grötzbach, G., Cacuci, D.G., 2001. 3D volume-of-fluid simulation of a wobbling bubble in a gas-liquid system of low Morton number. Proc. 4th Int. Conf. Multiphase Flow, May 27 – June 1, 2001, New Orleans, Louisiana, USA, CD-ROM.

Schubert, K., Brandner, J., Fichtner, M., Linder, G., Schygulla, U., Wenka, A., 2001. Microstructure devices for applications in thermal and chemical engineering. *Microscale Thermophysical Engineering* **5**, 17–39.

Sussman, M., Smereka, P., Osher, S., 1994. A level set approach for computing solutions to incompressible two-phase flow. *J. Comput. Phys*. **114**, 146-159.

Thulasidas, T.C., Abraham M.A., Cerro, R.L., 1995. Bubble train flow in capillaries of circular and square cross section. *Chem. Eng. Science* **50**, 183–199.

Univerdi, S.O., Tryggvason, G., 1992. A front-tracking method for viscous, incompressible, multi-fluid flows. *J. Comput. Phys.* **100**, 25-37.

Wörner, M., 2002. The influence of the gas-liquid density ratio on shape and rise velocity of an ellipsoidal bubble: a numerical study by 3D volume-of-fluid computations. Proc. 1st Int. Berlin Workshop on Transport Phenomena with Moving Boundaries, October 11–12, 2001, Berlin, Germany, F.-P. Schindler (Ed.), Fortschritt-Berichte VDI Reihe 3 Verfahrenstechnik Nr. 738, 67–84, VDI Verlag Düsseldorf.

Wörner, M., 2003. Invariance of the velocity field induced by a bubble rising steadily through liquid under variation of the gas-liquid density ratio. In: T. Schulenberg, M. Ozawa, G. Grötzbach (Eds.), Proc. German-Japanese Workshop on Multiphase Flow, Karlsruhe, Germany, August 25–27, 2002, Forschungszentrum Karlsruhe, FZKA 6759, March 2003, G10–G21. (http://bibliothek.fzk.de/zb/berichte/FZKA6759.pdf).

Wörner, M., Sabisch, W., Grötzbach, G., Cacuci, D.G., 2001. Volume-averaged conservation equations for volume-of-fluid interface tracking. Proc. 4th Int. Conf. Multiphase Flow, May 27 – June 1, 2001, New Orleans, Louisiana, USA, CD-ROM.

Wörner, M., Ghidersa, B.E., Shahab, A.F., 2004. Numerical study of bubble train flow in a square vertical mini-channel: influence of length of the flow unit cell. Proc. 5th Int. Conf. Multiphase Flow, May 30 – June 4, 2004, Yokohama, Japan, CD-ROM.